

Supporting Information

Elucidating the Structure-Dependent Selectivity towards Methane and Ethanol of CuZn in the CO₂ Electroreduction using Tailored Cu/ZnO Precatalysts

Seyedeh Behnaz Varandili,^a Dragos Stoian,^b Jan Vavra,^a Kevin Rossi,^a James R. Pankhurst,^a
Yannick T. Guntern,^a Núria López,^b Raffaella Buonsanti ^{a*}

^a Laboratory of Nanochemistry for Energy (LNCE), Institute of Chemical Sciences and Engineering, École Polytechnique Fédérale de Lausanne, CH-1950 Sion, Switzerland.

^b Institute of Chemical Research of Catalonia (ICIQ), The Barcelona Institute of Science and Technology, 43007 Tarragona, Spain

* Address correspondence to: raffaella.buonsanti@epfl.ch

Experimental Procedures

Chemicals

Zinc nitrate hexahydrate ($\text{Zn}(\text{NO}_3)_2 \cdot 6\text{H}_2\text{O}$, 99%), zinc stearate ($\{\text{CH}_3(\text{CH}_2)_{16}\text{COO}\}_2\text{Zn}$, 98%), copper(I)bromide ($\text{Cu}(\text{I})\text{Br}$, 99.99%), trioctylphosphine oxide ($[\text{CH}_3(\text{CH}_2)_7]_3\text{PO}$, or TOPO, 99%), oleylamine ($\text{C}_{17}\text{H}_{33}\text{NH}_2$ or OLAM, 70%), 1-octadecene ($\text{C}_{18}\text{H}_{36}$ or ODE, 90%) were all purchased from Sigma-Aldrich and used as received.

Synthesis of Cu/ZnO NCs

A previously developed procedure was utilized for the synthesis of the Cu/ZnO precatalysts, which are in the form of colloidal nanocrystals (NCs). 30 mL of an ODE solution containing ZnO seeds (13 nm or 60 nm, 0.5 mM) in a 100 mL three-necked flask were degassed under dynamic vacuum for 20 min at 130°C, after which they were heated under N_2 flow to 300°C for 5 minutes. ZnO seeds of 13 nm or 60 nm were used (**Fig. S1**). A copper precursor solution was prepared by mixing 0.1 mmol of $\text{Cu}(\text{OAc})$ and 0.4 mmol of TOP in degassed ODE (1.4 mL). 450 μL of this solution were then added dropwise to the flask containing the seeds at a rate of 0.18 mL/min using a syringe pump, during which time the reaction mixture slowly turned from colourless to brown. This amount of precursor corresponds to a Zn atomic content of 37% in the final samples. At the end of the injection, after around 150 s, the reaction was stopped, and the mixture was allowed to cool down to room temperature by removing the heating mantle. The NCs were extracted and purified by repeated washing/centrifugation cycles inside a N_2 glovebox to avoid Cu oxidation. 30 mL each of anhydrous EtOH and toluene were added to the reaction mixture at room temperature and the mixture was divided into four centrifugation vials; the particles were collected by centrifugation at 5000 rpm for 15 min. The precipitate was washed twice with EtOH to remove unreacted precursor and surfactants. Finally, the NCs were re-dispersed in hexane or toluene for storage.

Synthesis of ZnO nanocrystal (NC) seeds

Synthesis of 60 nm ZnO NCs (Fig. S1a)

1 mmol of $\text{Zn}(\text{NO}_3)_2 \cdot 6\text{H}_2\text{O}$ was mixed with 1 mL of OLAM in 6.3 mL of ODE at room temperature and dissolved at 80°C for 30 min. Nanocrystals were grown by heating the mixture to 260°C for 2 h. The as-prepared nanocrystals were purified by washing, precipitation and centrifugation, using ethanol, acetone and hexane in at least 4 cycles to remove any unreacted

zinc precursor, surfactants, and excess ODE. The resultant white precipitate was re-dispersed in hexane.

Synthesis of 13 nm ZnO NCs (Fig. S1b)

4 mmol of Zn(stearate)₂ and 30 mL OLAM were loaded into a 50 mL three-neck flask and degassed under vacuum for 10 min without stirring at room temperature and with vigorous stirring at 110°C. The mixture then was heated to 240°C and maintained at that temperature for 20 min under N₂. Afterward, it was cooled slowly by removing the heating mantle. The reaction products were precipitated by addition of acetone and centrifuged three times for 5 min at 5000 rpm. The final NCs were then re-dispersed and stored in hexane.

Synthesis of 25 nm Cu NCs (Fig. S1c).

1.5 mmol of CuBr and 25 mmol of TOPO were dissolved in 20 mL of OLAM in a three-necked flask with vigorous stirring. The resultant solution was heated to 80°C with a steep temperature ramp and maintained at this temperature for 15 min. Then, the temperature was raised to 230°C at a rate of 30°C/min and the solution was refluxed for 50 min before cooling to room temperature by removal of the heating mantle. The Cu NCs were purified by washing with ethanol, collecting the Cu NCs by centrifugation at 6000 rpm for 15 min. The resultant NCs were re-dispersed in hexane.

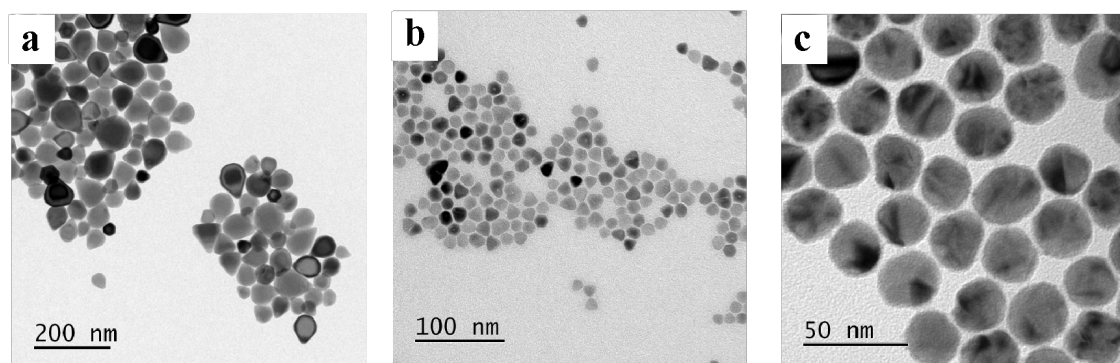


Fig. S1 Bright-field TEM images of (a) 60 nm ZnO NCs, (b) 13 nm ZnO NCs and (c) 25 nm Cu NCs.

Preparation of the Cu-ZnO physical mixture

The concentrations of ZnO seeds and Cu NCs with similar size and shape to those of hybrid nanocrystals (HNCs) in their stock solutions were determined by ICP-OES. Physical mixtures were then prepared by mixing Cu and ZnO NCs in a volumetric ratio such that the relative oxide and Cu concentrations in the mix mimicked those ratios found in compared HNCs.

Zn atomic percentage

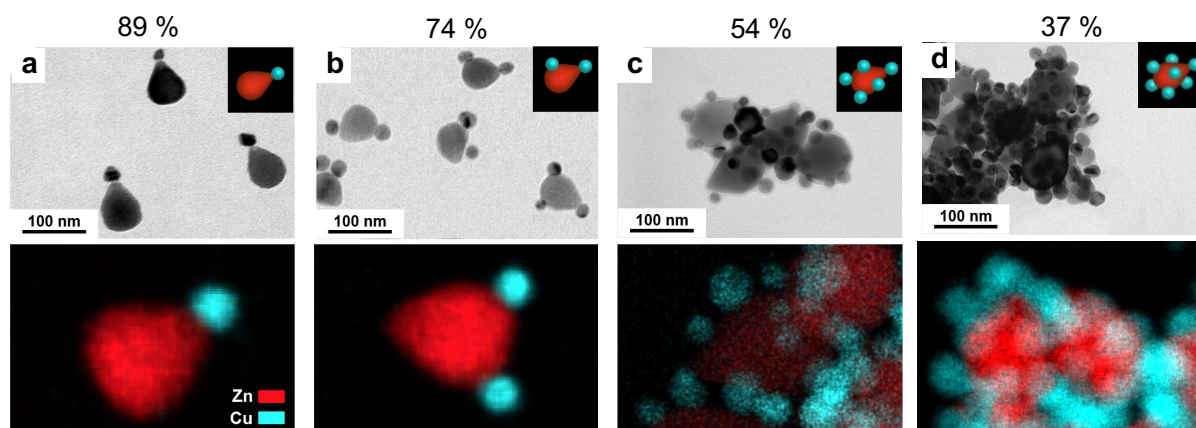


Fig. S2 Representative low-resolution TEM and EDXS elemental maps of ZnO@Cu NCs from 60 nm ZnO NC seeds with different Cu:Zn atomic ratios. The Cu:Zn atomic ratios were determined by ICP-OES.

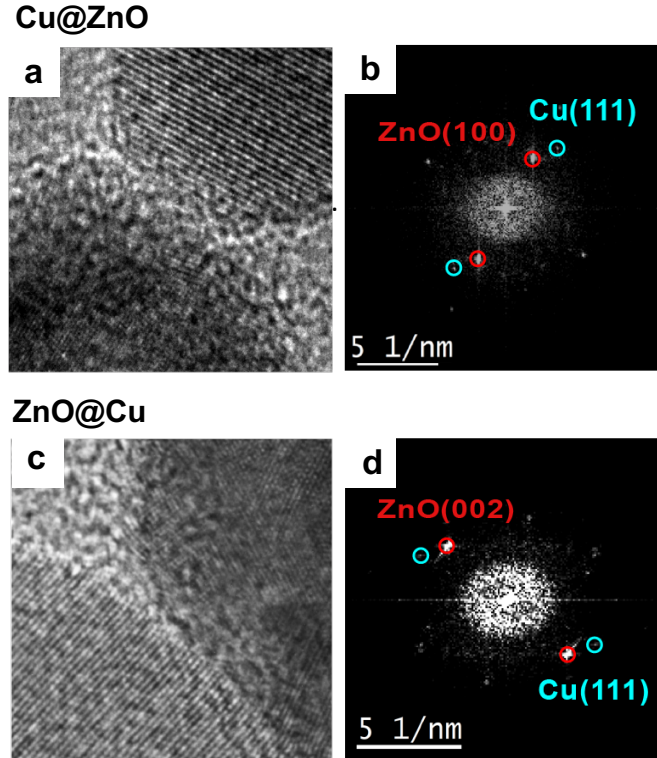


Fig. S3 HRTEM and corresponding FFT patterns of the interfacial region for (a,b) Cu@ZnO and (c,d) ZnO@Cu.

The mechanism of nucleation and growth of the HNCs was comprehensively discussed in our previous works.^{1,2} Herein, we further establish that the size of the ZnO seeds is a crucial parameter to switch from Cu@ZnO (**Fig. 1a,b**) to ZnO@Cu (**Fig. 1c,d**). The lattice mismatch between ZnO (wurtzite, hexagonal close-packed (hcp) with $a = 3.249$, $c = 5.204$ Å) and Cu (face-centred cubic (fcc) with $a = 3.61$ Å) can explain the partial wetting between the two domains instead of the formation of a core-shell structure, in agreement with the Volmer–Weber mechanism.³ When using the larger ZnO NCs as nucleation seeds for the growth of Cu domains, the ZnO@Cu configuration with small Cu domains decorating the central ZnO seeds is therefore expected. To explain the Cu@ZnO configuration obtained when smaller ZnO seeds are used instead, we speculate that the latter can no longer accommodate the interfacial strain triggered by the simultaneous nucleation of several Cu domains, so an unusual growth mechanism occurs where each Cu nucleus forms on multiple ZnO seeds.

The HRTEM images in **Fig. S3** focus on the interface in ZnO@Cu and Cu@ZnO NCs. The analysis shows that, although the two domains are intimately connected, no straightforward epitaxial relationship is present. The lattice spacings obtained from the fast Fourier transform (FFT) analysis on the interfacial region closely match those for the Cu (111) and the ZnO (002) for ZnO@Cu and the Cu (111) and ZnO (100) for Cu@ZnO NCs.

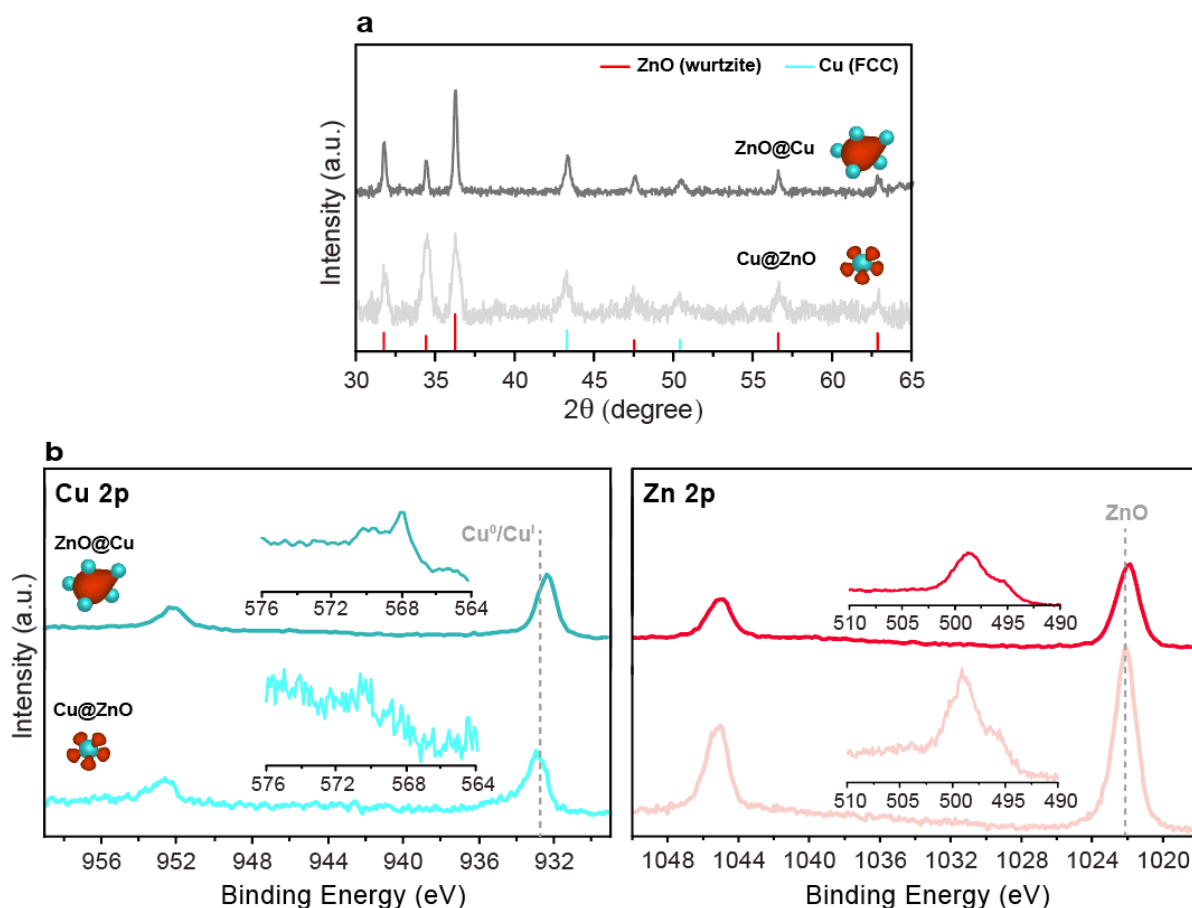


Fig. S4 (a) Representative normalized XRD patterns of the Cu/ZnO NCs. Reference patterns for ZnO (PDF #36-1451) and Cu (PDF #04-0836) are reported at the bottom of the graph. (b) XPS spectra of the Cu 2p region with Cu LMM spectra shown inset and the Zn 2p region with Zn LMM spectra shown inset. Note: the red and blue colors in the NC schemes represent the ZnO and Cu NCs, respectively)

In agreement with electron microscopy, the XRD patterns of the NCs (**Fig. S4a**) show two distinct sets of diffraction peaks arising from the fcc and hcp structure of Cu and ZnO, respectively. These results are indicative of the formation of distinct domains of metallic Cu and ZnO in the NCs and rule out the possibility of a CuZn alloy. The XPS results (**Fig. S4b**) revealed a similar state of Cu and Zn in both configurations. The Zn 2p and Zn LMM regions suggest that Zn is in its Zn^{2+} oxidation state. The absence of shakeup satellites in the Cu 2p plots of the samples excludes the presence of Cu^{2+} . The observed binding energy shifts in the Cu 2p spectra might be attributed to the different relative Cu^0/Cu^+ values. Regarding the Zn 2p, the shifts are mainly due to the particle size effect⁵ given the different size of the ZnO seeds in these samples.

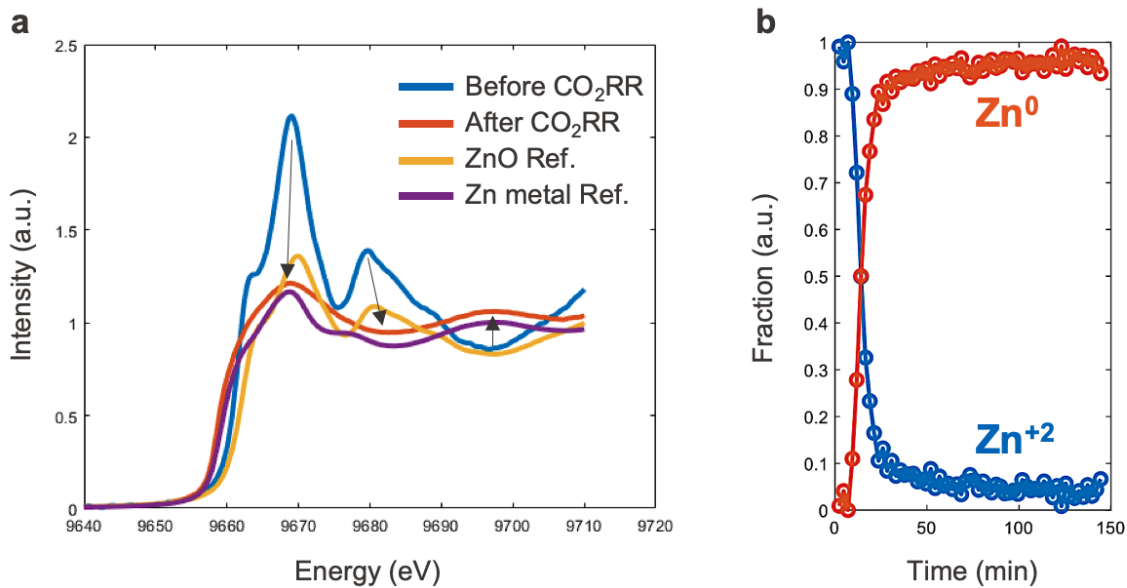


Fig. S5 (a) The Zn K-edge spectra of ZnO@Cu NCs before and after CO₂RR at -1.3 V_{RHE} together with the spectra of Zn and ZnO particles as references. (b) Concentration profiles of Zn⁰ and Zn²⁺ derived from the multivariate analysis of Zn K-edge XANES spectra

Operando XAS of the samples revealed that the drastic changes of the Cu/ZnO NCs during CO₂RR. The Zn K-edge XANES spectrum of as-synthesized ZnO@Cu NCs first resembles that of ZnO but transforms to metallic Zn during CO₂RR at -1.3 V_{RHE} (**Fig. S5a**). **Fig. S5b** reports the changes in the fraction of Zn⁰ and Zn²⁺ as extracted from XANES spectra. Similar behaviour was observed at -1.1 V_{RHE} and -1.2 V_{RHE}

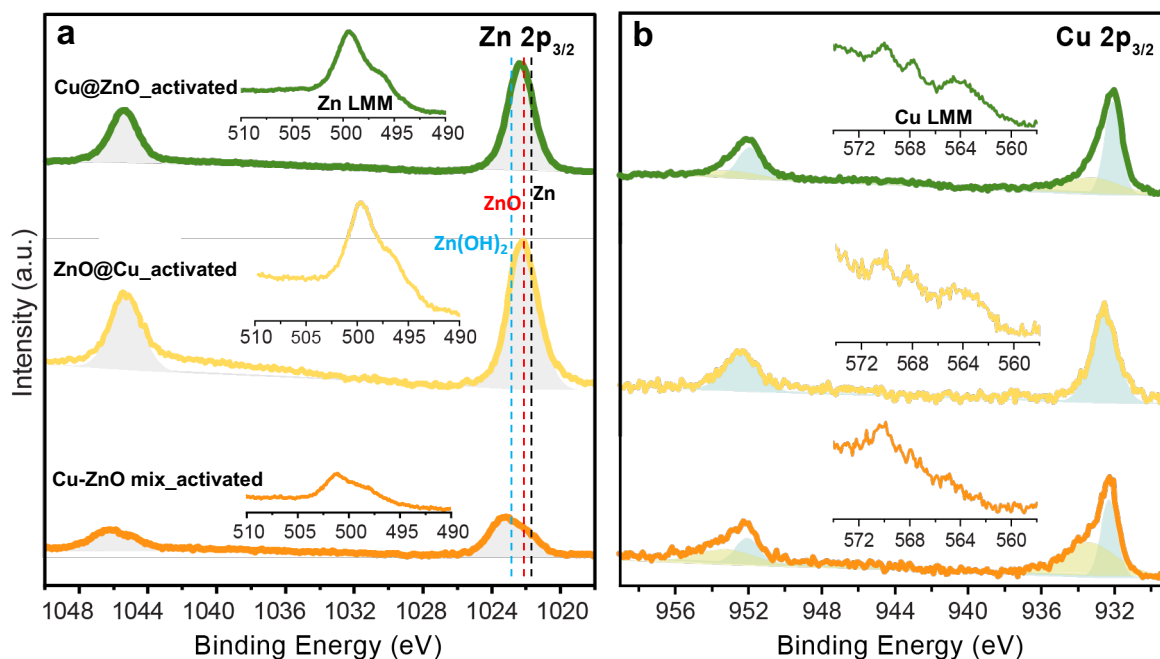


Fig. S6 XPS spectra showing (a) the Zn 2p_{3/2} and Zn LMM regions (the latter are inset) and (b) the Cu 2p_{3/2} and Cu LMM regions (the latter are inset) for activated Cu@ZnO and ZnO@Cu; the Cu-ZnO mixture is shown for comparison.

In agreement with the EDXS mapping, the XPS results (**Fig. S6** and **Table S1**) indicate an increase of the Zn:Cu ratio on the surface of the NCs after the activation step, which is particularly evident in the case of ZnO@Cu. Instead, this ratio decreased slightly in the case of the Cu-ZnO mixture. In order to comment on the charge transfer between the Cu and ZnO domains and their oxidation state, we examined the 2p_{3/2} binding energies (E_b) as well as the modified Auger parameters (a'), which is independent of calibration and energy of the X-ray source, which might otherwise cause fictitious peak shifts.⁴

Table S1. Modified Auger parameter (a') of Cu, Zn as well as the Zn:Cu ratio for the samples before and after activation. $a' = E_k(M_{LMM}) + E_b(M_{2p_{3/2}})$, where M = Cu or Zn.

Sample	a'_{Cu} (eV)	a'_{Zn} (eV)	Zn/Cu
as-synthesized Cu@ZnO	1849.4	2009.71	3
activated Cu@ZnO	1848.69	2009.6	3.4
as-synthesized ZnO@Cu	1849.22	2009.96	1.29
activated ZnO@Cu	1848.59	2009.06	4.72
as-synthesized Cu-ZnO mix	1850.05	2009.95	0.94
activated Cu-ZnO mix	1848.74	2008.78	0.82

From comparisons with Wagner plots for Zn, the a'_{Zn} and Zn 2p_{3/2} binding energies of both NCs suggest the presence of ZnO on the surface after activation, which is expected due to the inevitable short exposure to air after activation. The values of a'_{Cu} and Cu 2p_{3/2} binding energies for Cu in all samples are consistent with the co-presence of Cu⁰ and Cu⁺ after activation, with the Cu⁰:Cu⁺ ratio being slightly higher for the ZnO@Cu NCs. The significant shift in a'_{Zn} and Zn 2p_{3/2} for activated Cu-ZnO mix might be due to the formation of Zn(OH)₂ species after activation, which is not observed for the Cu/ZnO NCs.

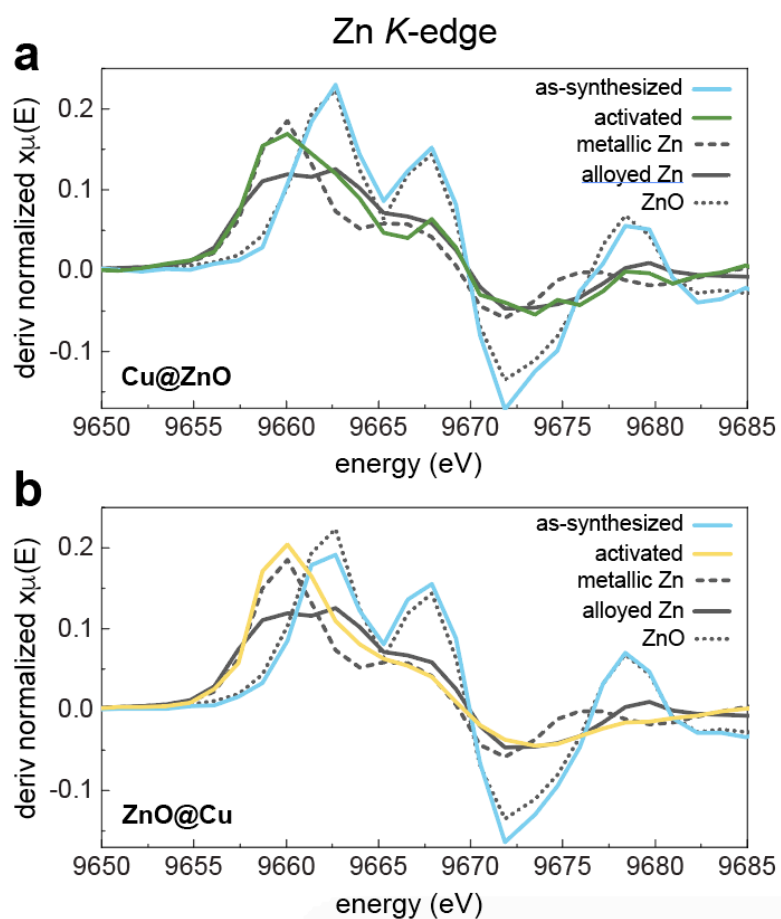


Fig. S7 First-order derivative Zn K-edge XANES spectra of (a) Cu@ZnO, (b) ZnO@Cu NCs before and after activation at $-1.1 V_{RHE}$.

The data in **Fig. S7** are consistent with metallic Zn with some contribution from alloyed Zn indicated by the presence of the satellite peak at ca. 9680 eV

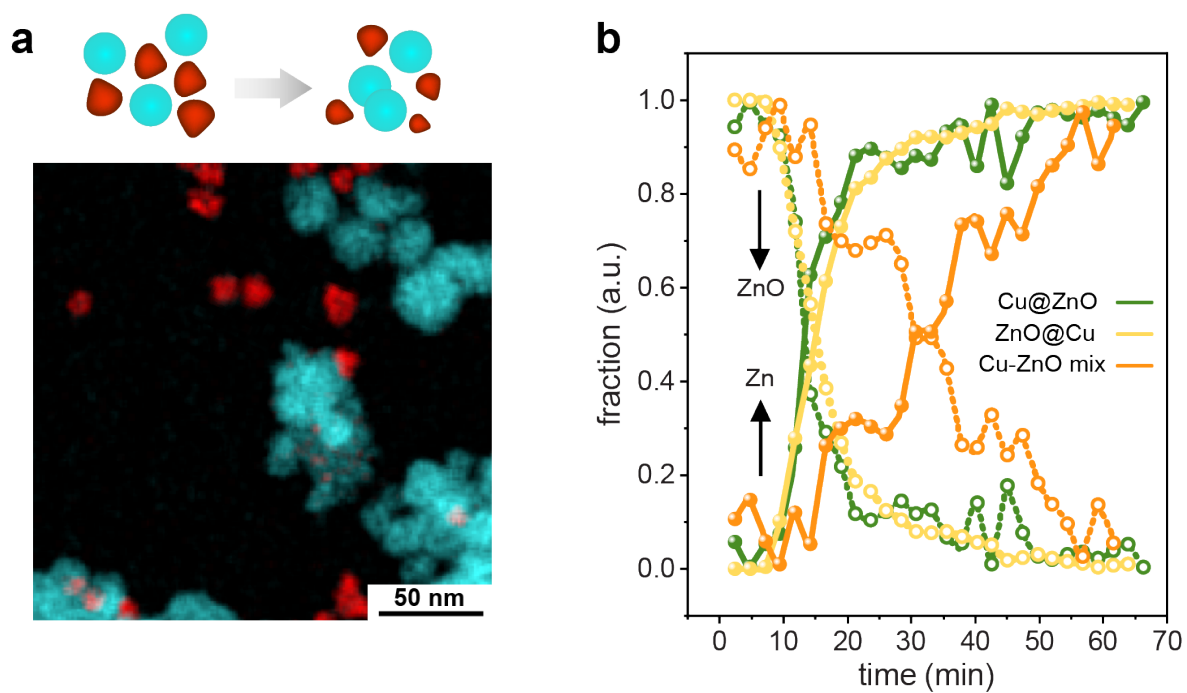


Fig. S8 (a) Schematic of the morphological evolution during activation and corresponding EDXS elemental maps for Cu-ZnO mix after activation at $-1.1 \text{ V}_{\text{RHE}}$ for 1 hour. (b) Comparison of concentration changes of Zn^0 and Zn^{2+} in Cu/ZnO NCs and Cu-ZnO mix derived from the multivariate analysis of Zn K-edge XANES spectra of the samples during activation at -1.1 V vs RHE.

Electrocatalytic Measurements

Electrochemical Active Surface Area (ECSA)

Double-layer capacitance measurements were carried out on the samples in order to assess their surface areas. Using CO₂ saturated 0.1 M KHCO₃, cyclic voltammograms (CVs) were recorded at scan rates of 4, 8, 12, 16, 20, 24, 28 and 32 mV s⁻¹. A potential range of -0.15 to -0.2 V vs Ag/AgCl was chosen due to the absence of any Faradaic redox processes at these potentials. For each CV, the geometric current-densities at -0.18 V vs Ag/AgCl were recorded for both the cathodic ($J_{geom.,cath.}$) and anodic ($J_{geom.,anod.}$) sweeps; the difference between these two values gives a total value ($J_{geom.,T}$) for each scan rate (**Eq. S1**).

$$J_{geom.,T} = J_{geom.,anod.} - J_{geom.,cath.} \quad \text{Eq. S1}$$

These current densities ($J_{geom.,T} / \mu\text{A cm}^{-2}$) were plotted against the increasing scan rates ($v / \text{V s}^{-1}$) to yield a linear plot whose slope gives the electrochemical double-layer capacitance ($C_{ECDL, sample} / \mu\text{F cm}^{-2}$; R^2 typically greater than 0.99). By carrying out the same process for a clean glassy-carbon electrode, a reference capacitance value is obtained ($C_{ECDL, ref.} / \mu\text{F cm}^{-2}$) from which a surface-roughness factor can be obtained (SRF, **Eq. S2**). By assuming the C_{ECDL} changes due to changes in the surface area (by addition of a nanomaterial to the substrate), the SRF can be multiplied by the geometric surface area ($A_{geom.} / \text{cm}^2$) to give a more accurate value (A_{ECSA} / cm^2 ; **Eq. S3**).

$$SRF = \frac{C_{ECDL, sample}}{C_{ECDL, ref.}} \quad \text{Eq. S2}$$

$$A_{ECSA} = SRF \times A_{geom} \quad \text{Eq. S3}$$

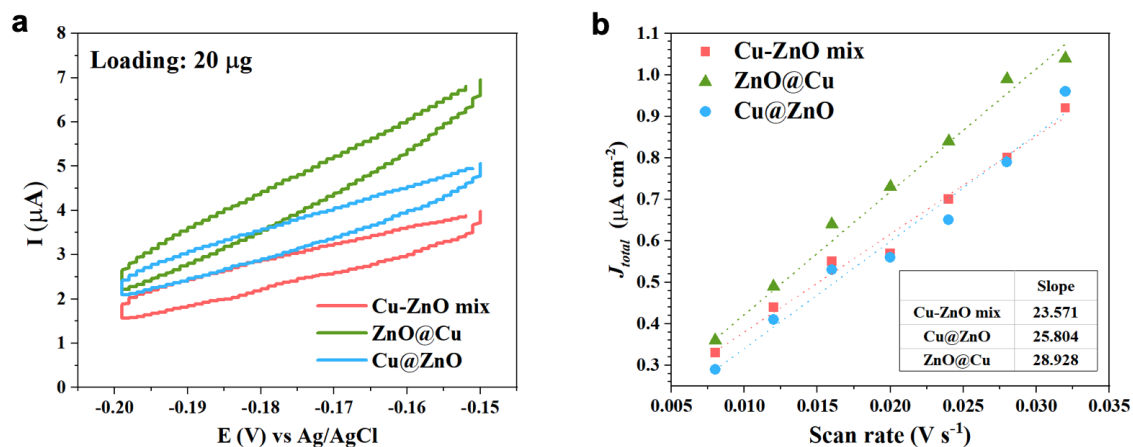


Fig. S9 (a) Cyclic voltammograms of activated ZnO@Cu, Cu@ZnO and the Cu-ZnO mixture ($20 \mu\text{g}_{\text{Cu}}$ each) in 0.1 M KHCO_3 saturated with CO_2 , measured at 20 mV s^{-1} . (b) Current dependence on scan rate of the aforementioned NCs. The slopes indicate the electrochemical double-layer capacitance for each sample. Note: each point of the plots in Fig. b was calculated by subtraction of anodic and cathodic currents at $-0.18 \text{ V}_{\text{Ag}/\text{AgCl}}$ for each scan rate.

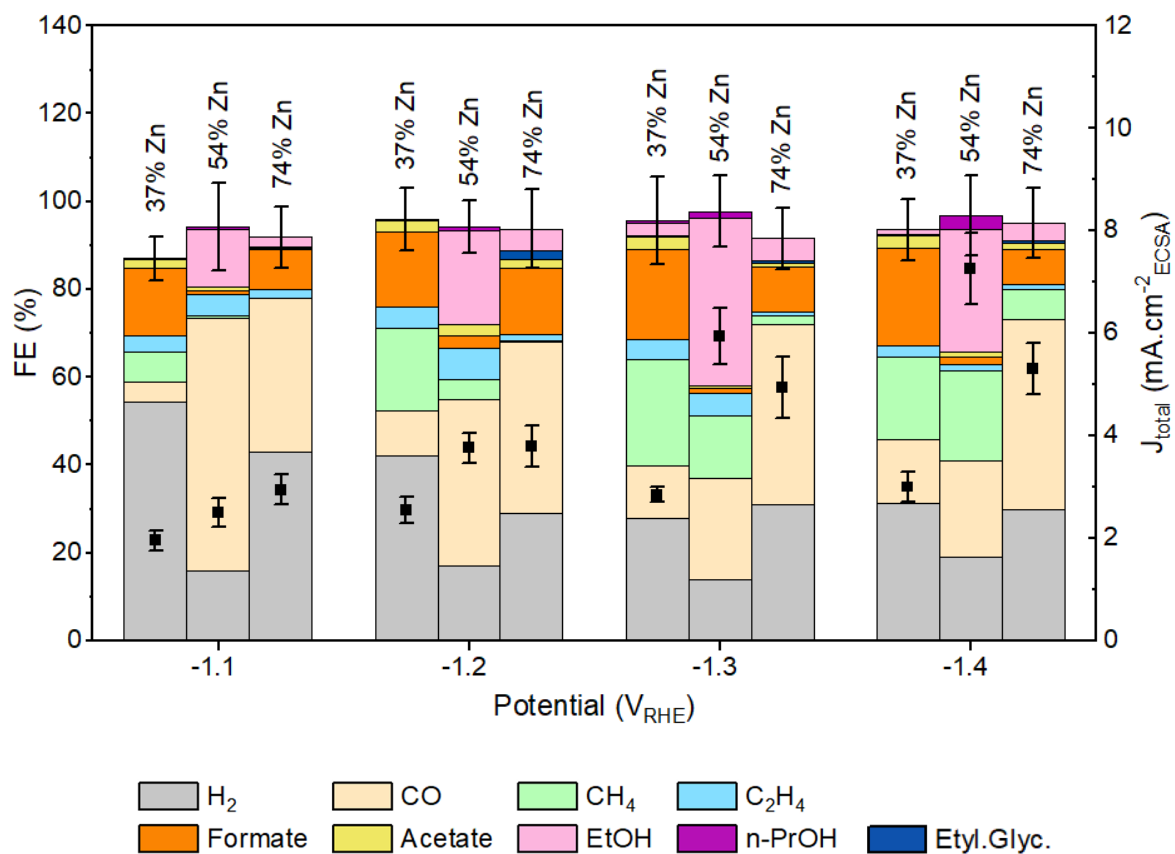


Fig. S10 Faradaic efficiencies and the total current densities at variable potentials for 20 μg of activated ZnO@Cu with variable Cu:Zn ratios loaded on a glassy carbon surface of 1 cm^2 . The error bars for total FE and J_{total} correspond to the standard deviation from three independent measurements.

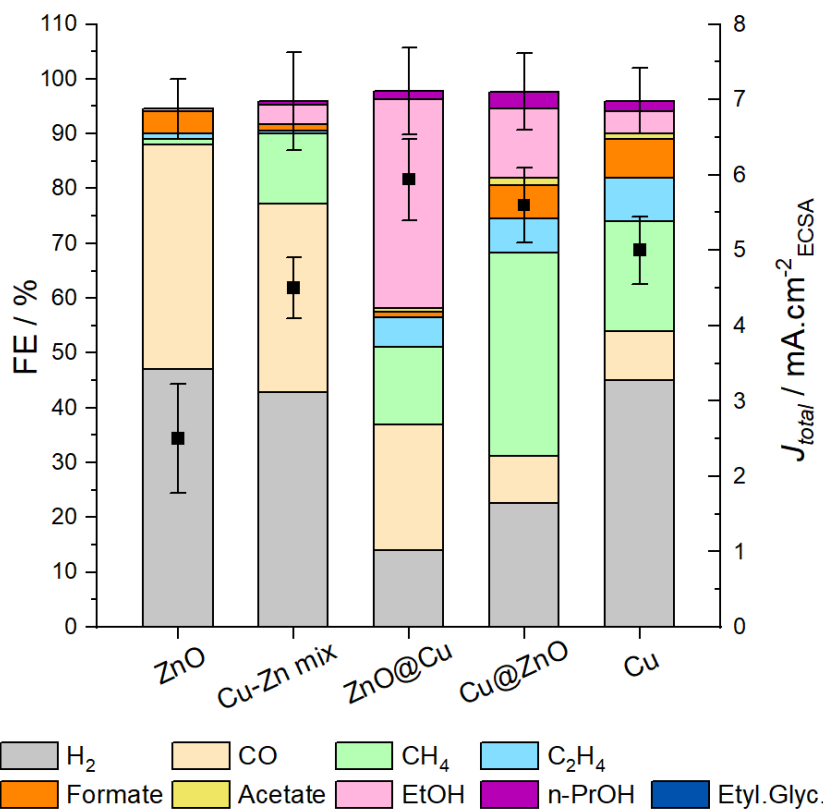


Fig. S11 FE and the total current densities ($J_{total} = J_{CO_2RR+HER}$) for 20 μg of activated ZnO, Cu-ZnO mix, ZnO@Cu, Cu@ZnO and Cu NCs of 25 nm loaded on a glassy carbon surface of 1 cm^2 , measured at -1.3 V_{RHE} . The error bars for total FE and J_{total} correspond to the standard deviation from three independent measurements

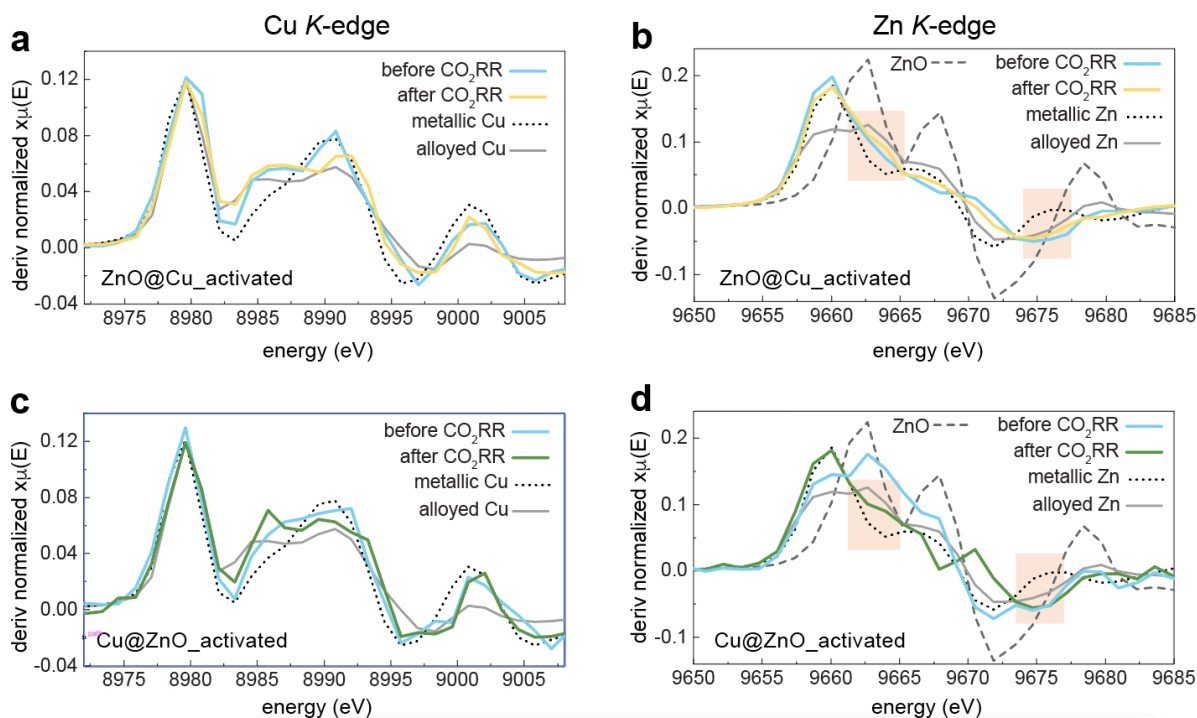


Fig. S12 First-order derivative of Cu K-edge (left column) and Zn K-edge (right column) XANES spectra for the activated (a,b) Cu@ZnO and (c,d) ZnO@Cu at $-1.3 V_{\text{RHE}}$ for 2.5 hour.

Fig. S12 reports the first-order derivative of the Cu and Zn K-edge spectra from operando measurements before and after CO_2RR . Subtle changes are observed for Cu (**Fig. S12 a,c**). A qualitative assessment of the final Cu K-edge spectrum after CO_2RR evidence that the degree of alloyed Cu in the activated ZnO@Cu is slightly higher compared to activated Cu@ZnO. The Zn K-edge of the activated ZnO@Cu does not undergo substantial changes before and after CO_2RR (**Fig. S12b**). Instead, for Cu@ZnO (**Fig. S12d**) the Zn re-oxidizes in the timeframe between the activation and the start of CO_2RR (around 10 minutes at open circuit voltage) before getting again reduced to metallic Zn after CO_2RR . During CO_2RR , the alloying process between Cu and Zn continues as the spectra of the two catalysts become closer to the Cu-Zn alloy reference. However, it should be noted that a fraction of metallic state of both elements (specially Zn) are still present in the samples after CO_2RR (The red squares in Zn K-edge plots, highlight the resemblance of sample spectra to each metallic and alloyed references of Zn).

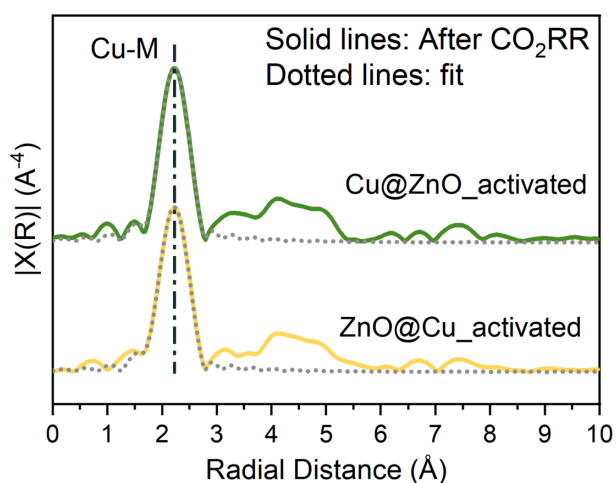


Fig. S13 FT k^2 -weighted Cu K-edge EXAFS data and fitting results for the activated Cu@ZnO and ZnO@Cu after CO₂RR reaction at $-1.3 V_{\text{RHE}}$ for 2.5 hours.

Additional information on the Cu and Zn coordination environment and interatomic distances were provided by the Fourier-transformed (FT) Cu K-edge EXAFS spectra of the samples after CO₂RR (**Fig. S13**). Consistent with the XANES results, there is no evidence of Cu–O peaks in the EXAFS spectra after the CO₂RR reaction. Instead, a strong feature appears around 2.1–2.2 Å which can be assigned to the Cu–M bonds. Because of the close electronic structure of Cu and Zn, the differentiation between Cu–Cu and Cu–Zn bonds is challenging. However, the Cu–M interatomic distances in all samples were shorter than the Cu–Cu bonds in Cu foil (2.56 Å). This finding suggests that the catalysts are pure Cu. Furthermore, the Cu–M interatomic distance is slightly bigger for Cu@ZnO ($2.544 \text{ Å} \pm 0.005$) than for ZnO@Cu ($2.548 \text{ Å} \pm 0.006$). This observation is consistent with the expansion of the fcc-type lattice through partial alloying with Zn,^{5,6} and suggests that a higher fraction of Cu–Zn bonds is present in the ZnO@Cu. Concomitantly, the Cu@ZnO possess a slightly lower coordination (9.1 ± 0.7) compared to ZnO@Cu (10.2 ± 0.9). The presence of lower-coordinated sites might contribute toward stabilization of oxide species within the structure as discussed in the literature, which is then in line with a less degree of alloying.⁷ However, it should be noted that since the CuZn bimetallic interactions are only limited to the surface of NCs, tiny differences in Cu–M bond lengths are expected, given the fact that the XAS techniques provide information not on the local but on the average structure of the NCs.

DFT Surface Energetics

To infer whether the Zn atom is more likely to sit on surface or subsurface sites we calculate its segregation energies E_{seg} ⁸: $E_{\text{seg}} = E_{\text{Cu-Zn,surface}} - E_{\text{Cu-Zn,subsurface}}$ (1)

Where $E_{\text{Cu-Zn,surface}}$ and $E_{\text{Cu-Zn,subsurface}}$ label respectively the total energy of the (111) slab where Zn lies on a surface or subsurface site. As illustrated in **Fig. S14a**, we find that E_{seg} is negative and small in magnitude ($E_{\text{seg}} = -0.12$ eV). The small energy difference reflects in an almost equal probability of finding the two states at 300K, with subsurface Zn slightly favoured w.r.t. surface Zn.

To rationalize the tendency of Zn atoms to cluster together we calculate their islanding energies E_{isl} ⁹: $E_{\text{isl}} = E_{\text{dimer}} - E_{\text{separated}}$ (2)

Where E_{dimer} and $E_{\text{separated}}$ label respectively the total energy of the (111) slab where two Zn lie on neighbouring site. As illustrated in **Fig. S14b**, we find that E_{isl} is small and negative in magnitude ($E_{\text{isl}} = -0.04$ eV). The small energy difference reflects in an almost equal probability of finding the two states at 300K, with dimerized Zn slightly unfavoured w.r.t. separated Zn atoms.

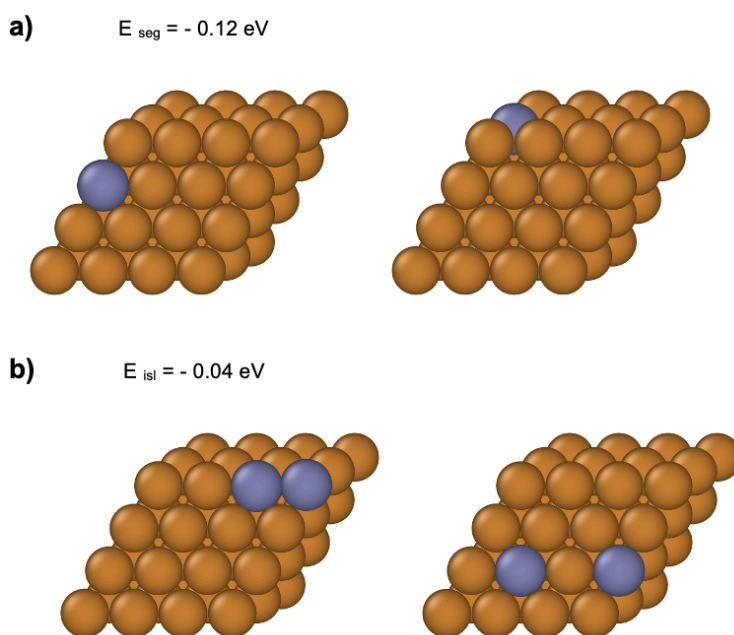


Fig. S14 Snapshots of the 4x4x4 (111) slabs utilized to evaluate segregation tendencies (a) and islanding tendencies (b) of Zn atoms. Brown and grey spheres indicate Cu and Zn atoms, respectively

DFT ΔE_{COH} Energetics

We calculate the formation energy of COH from adsorbed CO, ΔE_{COH} , within the computational hydrogen electrode model:

$$\Delta E_{COH} = E_{COH^*} - E_{CO^*} - E_{H_2}/2 \quad (3)$$

Where E_{COH} and E_{CO} is the energy found for adsorbed CO and COH on the catalyst and E_{H_2} is the energy of an H_2 molecule in the gas phase.

We calculate the d-band centre of the adsorption site,^{9,10} ε , as:

$$\varepsilon = \frac{\int_{-\infty}^{EF} \rho(x) x dx}{\int_{-\infty}^{EF} \rho(x) dx} \quad (4)$$

Where EF labels the Fermi Energy, $\rho(x)$ the electronic density of state distribution, and x runs over the energy levels.

We evaluate the Bader charge density of the adsorption site,¹¹ δ , utilizing the algorithm and code developed by Henkelman and coworkers.¹²

In **Fig. S15-S16** we report a breakdown of ΔE_{COH} , ε , and δ found for different non-equivalent adsorption sites and systems, characterized by the number and location of Zn atoms in their neighbourhood.

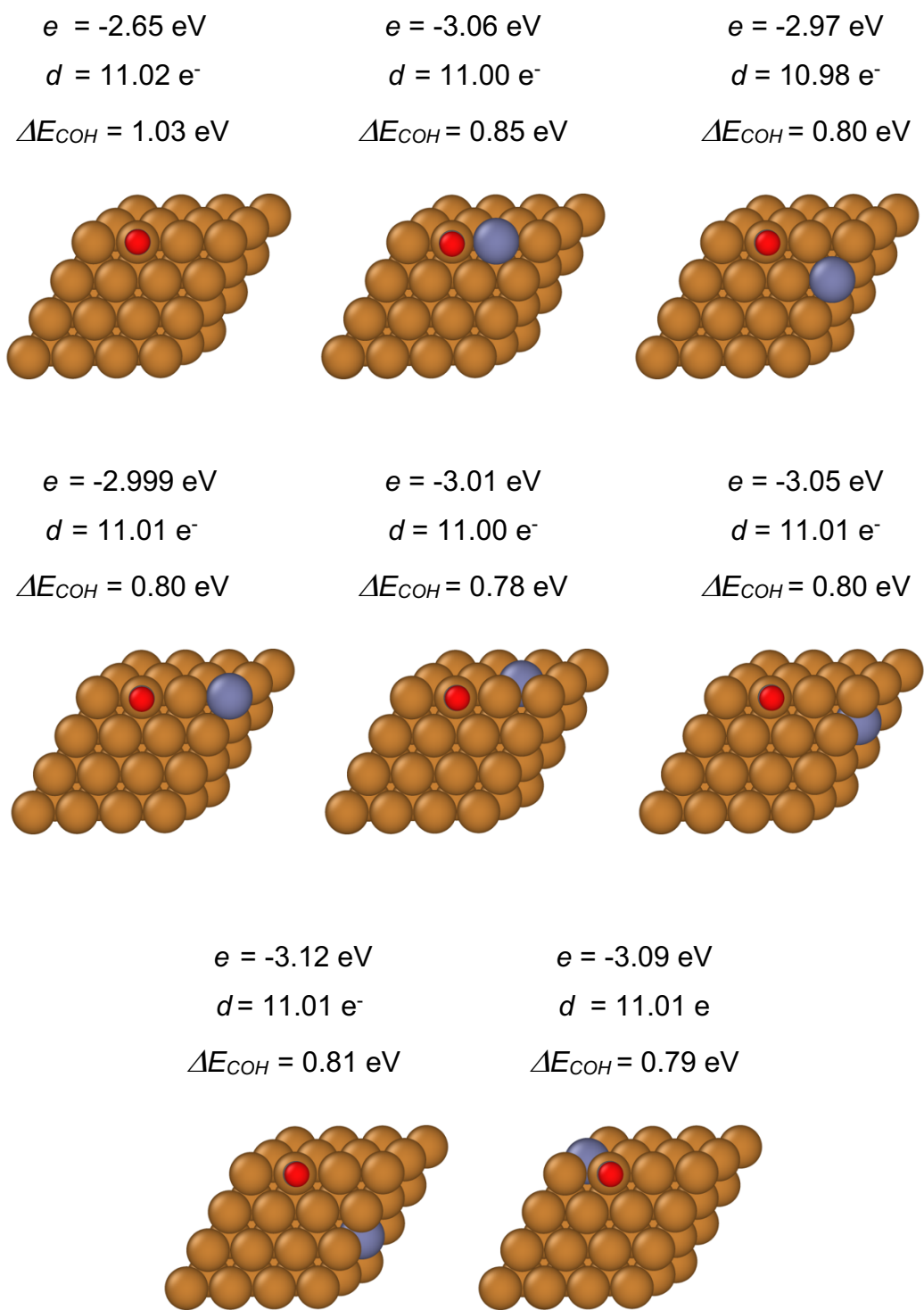


Fig. S15 Set of configurations utilized to evaluate of the effect of zero and one Zn impurities on CO protonation energetics. Together with their 3D representation we also report ΔE_{COH} (eV). Because of the combinatorial nature of the problem, we do not address the systematic enumeration and evaluation of adsorption energies in systems with multiple impurities but rather consider few paradigmatic examples.

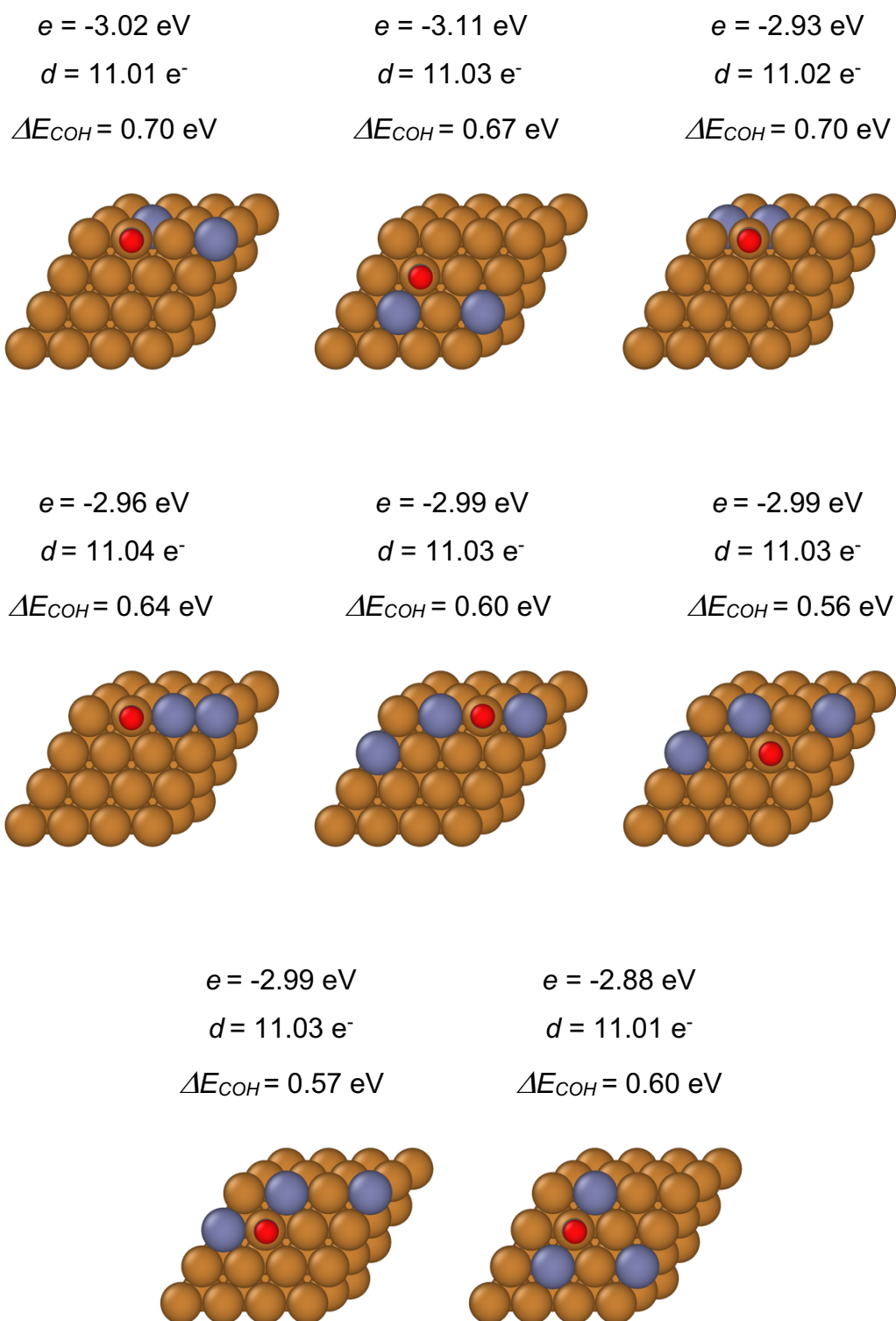


Fig. S16 Set of configurations utilized to evaluate the effect of two and three Zn impurities on CO protonation energetics. Together with their 3D representation we also report ΔE_{COH} (eV). Because of the combinatorial nature of the problem, we do not address the systematic enumeration and evaluation of adsorption energies in systems with multiple impurities but rather consider few paradigmatic examples.

DFT ΔE_{CO-CO^*} Energetics

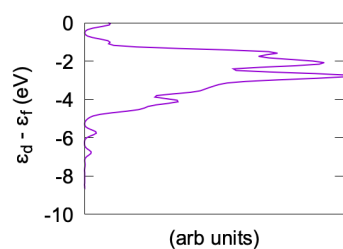
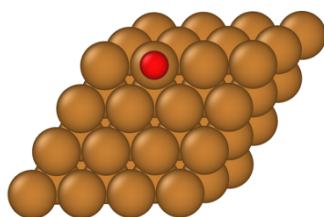
We calculate the difference in energy between bound and unbound CO, ΔE_{CO-CO^*} :

$$\Delta E_{CO-CO^*} = E_{CO} + E_{surf} - E_{CO^*} \quad (5)$$

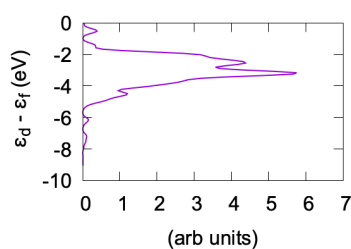
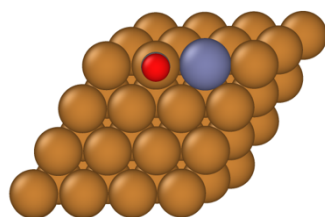
Where E_{CO} labels the energy of CO in gas phase, E_{surf} the energy of the catalysts, and E_{CO^*} the energy found for CO adsorbed on the catalysts.

In **Fig. S17-S19**, we report a breakdown of ΔE_{CO-CO^*} , ε , and δ found for different non-equivalent adsorption sites and systems, characterized by the number and location of Zn atoms in their neighbourhood.

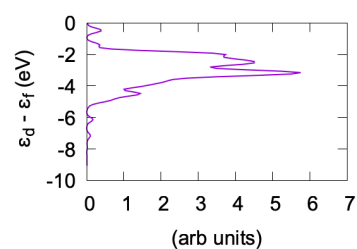
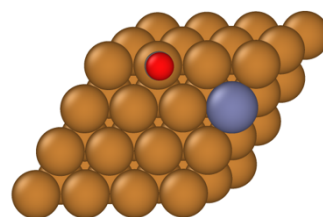
$\varepsilon = -2.65 \text{ eV}$
 $d = 11.23 \text{ e}^-$
 $\Delta E_{CO-CO^*} = 0.85 \text{ eV}$



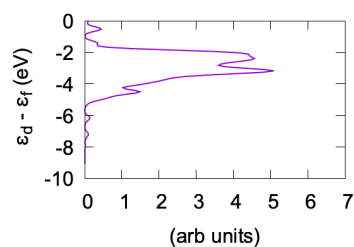
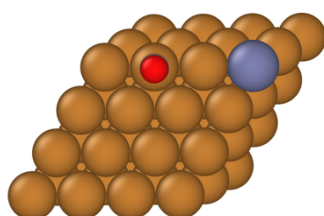
$\varepsilon = -3.06 \text{ eV}$
 $d = 11.00 \text{ e}^-$
 $\Delta E_{CO-CO^*} = 0.95 \text{ eV}$



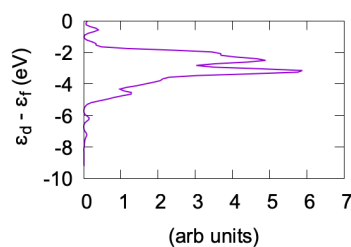
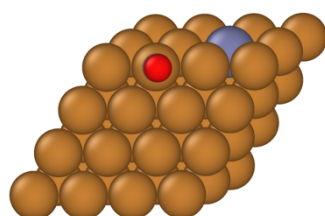
$\varepsilon = -2.97 \text{ eV}$
 $d = 10.98 \text{ e}^-$
 $\Delta E_{CO-CO^*} = 0.94 \text{ eV}$



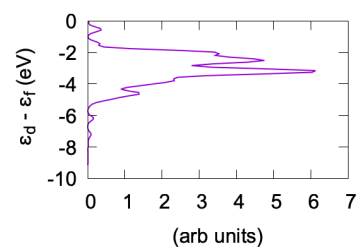
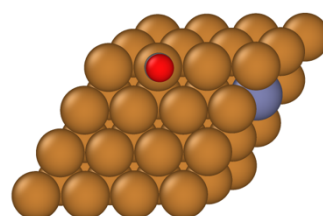
$\varepsilon = -2.99 \text{ eV}$
 $d = 11.01 \text{ e}^-$
 $\Delta E_{CO-CO^*} = 0.94 \text{ eV}$



$\varepsilon = -3.01 \text{ eV}$
 $d = 11.0 \text{ e}^-$
 $\Delta E_{CO-CO^*} = 0.94 \text{ eV}$



$\varepsilon = -3.05 \text{ eV}$
 $d = 11.01 \text{ e}^-$
 $\Delta E_{CO-CO^*} = 0.88 \text{ eV}$



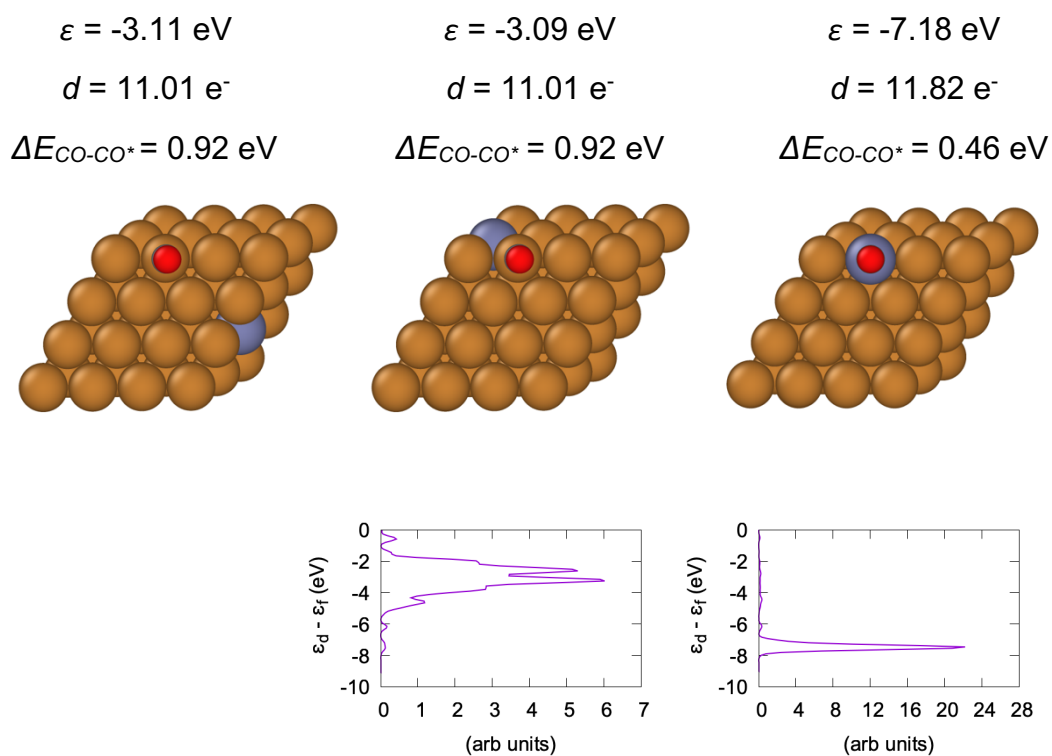
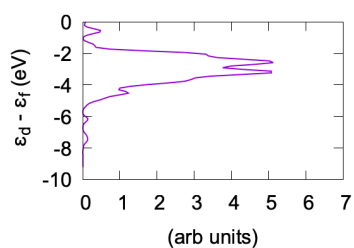
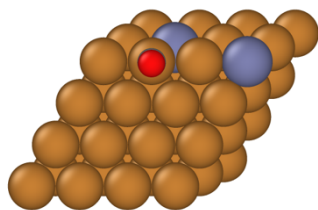
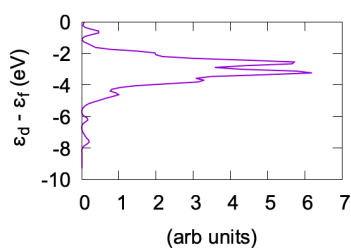
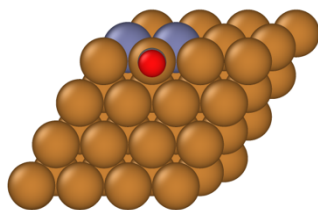


Fig. S17 Set of configurations utilized to evaluate the effect of zero and one Zn impurities on CO protonation energetics. Together with their 3D representation we also report ΔE_{CO-CO^*} (eV), Bader Charge d , d-band center ε , and Projected Density of States (PDOS). Because of the combinatorial nature of the problem, we do not address the systematic enumeration and evaluation of adsorption energies in systems with multiple impurities but rather consider a few paradigmatic examples.

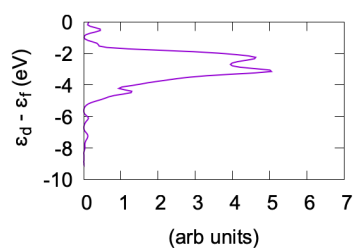
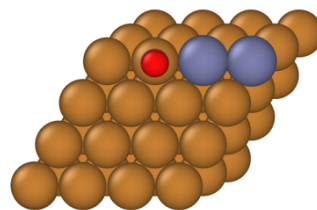
$\epsilon = -3.02 \text{ eV}$
 $d = 11.01 \text{ e}^-$
 $\Delta E_{\text{CO-CO}^*} = 0.98 \text{ eV}$



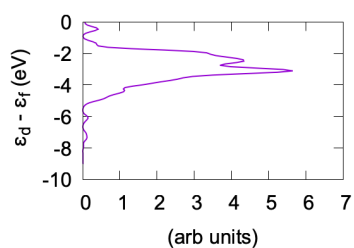
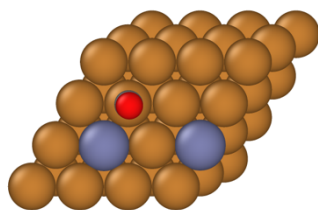
$\epsilon = -3.11 \text{ eV}$
 $d = 11.03 \text{ e}^-$
 $\Delta E_{\text{CO-CO}^*} = 1.00 \text{ eV}$



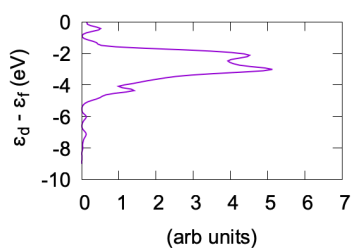
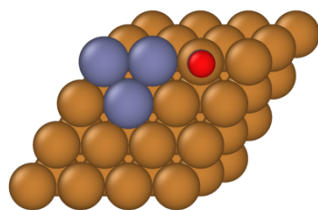
$\epsilon = -2.93 \text{ eV}$
 $d = 11.02 \text{ e}^-$
 $\Delta E_{\text{CO-CO}^*} = 1.01 \text{ eV}$



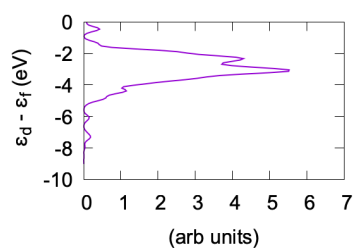
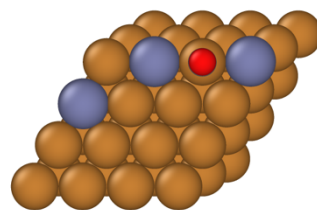
$\epsilon = -2.96 \text{ eV}$
 $d = 11.04 \text{ e}^-$
 $\Delta E_{\text{CO-CO}^*} = 1.04 \text{ eV}$



$\epsilon = -2.84 \text{ eV}$
 $d = 11.07 \text{ e}^-$
 $\Delta E_{\text{CO-CO}^*} = 0.92 \text{ eV}$



$\epsilon = -2.99 \text{ eV}$
 $d = 11.03 \text{ e}^-$
 $\Delta E_{\text{CO-CO}^*} = 0.96 \text{ eV}$



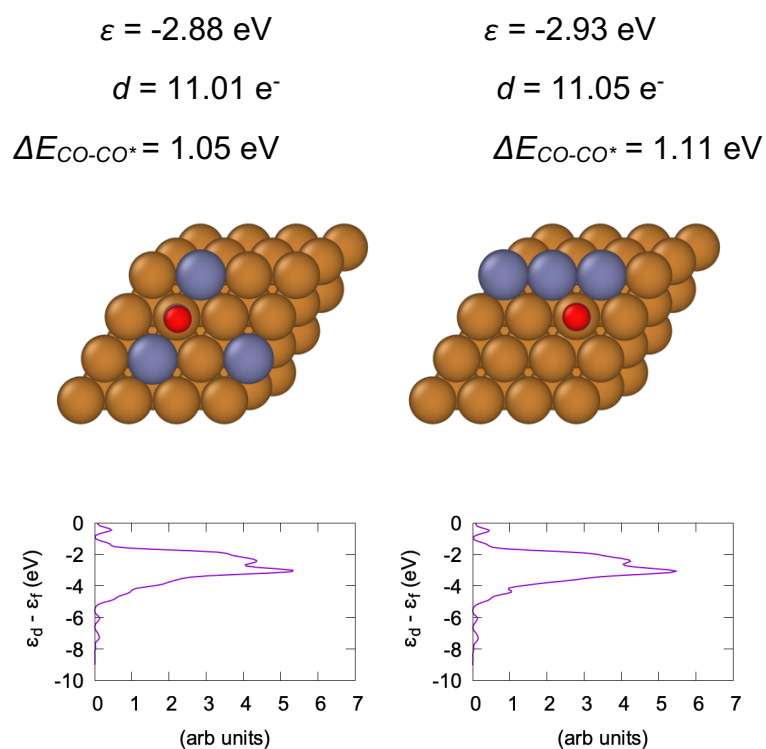
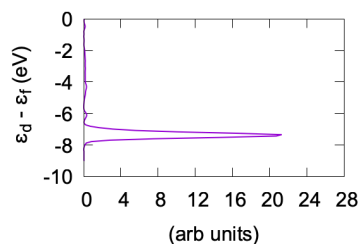
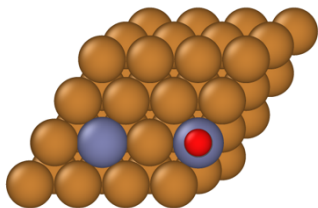
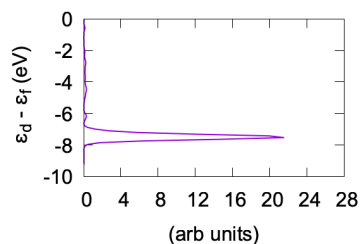
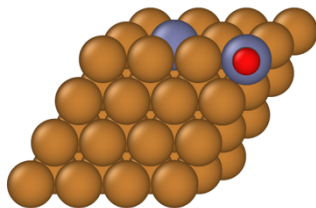


Fig. S18 Set of configurations utilized to evaluate the effect of two and three Zn impurities on CO protonation energetics. Together with their 3D representation we also report $\Delta E_{\text{CO-CO}^*}$ (eV), Bader Charge d , d-band center ε , and Projected Density of States (PDOS). Because of the combinatorial nature of the problem, we do not address the systematic enumeration and evaluation of adsorption energies in systems with multiple impurities but rather consider a few paradigmatic examples.

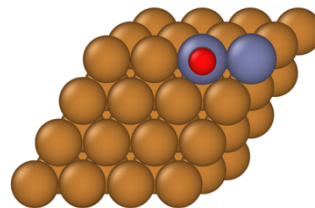
$\varepsilon = -6.98 \text{ eV}$
 $d = 11.82 \text{ e}^-$
 $\Delta E_{\text{CO-CO}^*} = 0.52 \text{ eV}$



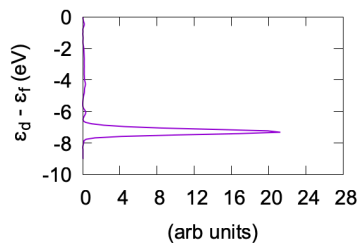
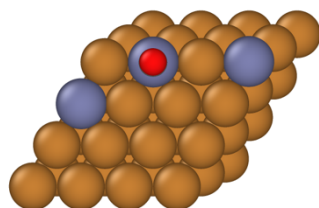
$\varepsilon = -6.94 \text{ eV}$
 $d = 11.84 \text{ e}^-$
 $\Delta E_{\text{CO-CO}^*} = 0.52 \text{ eV}$



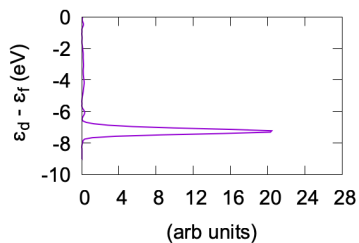
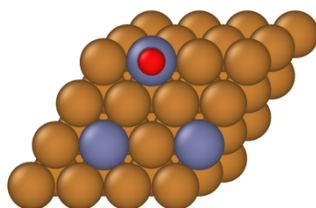
$\varepsilon = -7.04 \text{ eV}$
 $d = 11.83 \text{ e}^-$
 $\Delta E_{\text{CO-CO}^*} = 0.56 \text{ eV}$



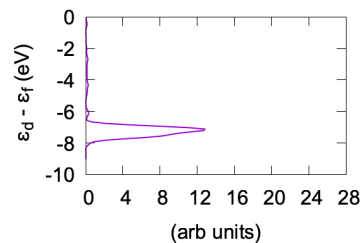
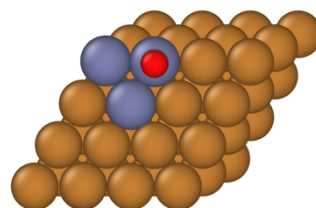
$\varepsilon = -6.94 \text{ eV}$
 $d = 11.84 \text{ e}^-$
 $\Delta E_{\text{CO-CO}^*} = 0.61 \text{ eV}$



$\varepsilon = -7.00 \text{ eV}$
 $d = 11.83 \text{ e}^-$
 $\Delta E_{\text{CO-CO}^*} = 0.47 \text{ eV}$



$\varepsilon = -6.98 \text{ eV}$
 $d = 11.88 \text{ e}^-$
 $\Delta E_{\text{CO-CO}^*} = 0.63 \text{ eV}$



$$\varepsilon = -7.04 \text{ eV}$$

$$d = 11.89 e^-$$

$$\Delta E_{CO-CO^*} = 0.65 \text{ eV}$$

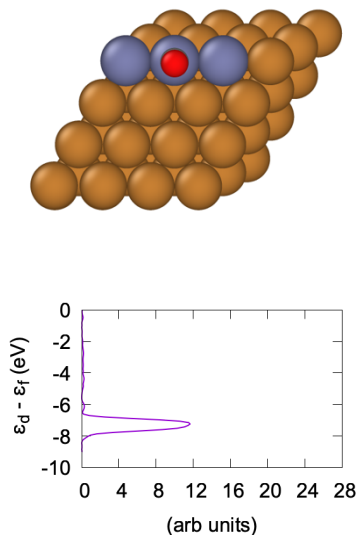


Fig. S19 Set of configurations utilized to evaluate the effect of two and three Zn impurities on CO energetics. Together with their 3D representation we also report ΔE_{CO-CO^*} (eV), Bader Charge d , d-band center ε , and Projected Density of States (PDOS). Because of the combinatorial nature of the problem, we do not address the systematic enumeration and evaluation of adsorption energies in systems with multiple impurities but rather consider few paradigmatic exampl

References

- 1 S. B. Varandili, J. Huang, E. Oveisi, G. L. De Gregorio, M. Mensi, M. Strach, J. Vavra, C. Gadiyar, A. Bhowmik and R. Buonsanti, *ACS Catal.*, 2019, **9**, 5035–5046.
- 2 S. B. Varandili, D. Stoian, J. Vavra, J. Pankhurst and R. Buonsanti, *Chem. Sci.*, 2020, **11**, 13094–13101.
- 3 M. Casavola, R. Buonsanti, G. Caputo and P. D. Cozzoli, *Eur. J. Inorg. Chem.*, 2008, **2008**, 837–854.
- 4 M. C. Biesinger, *Surf. Interface Anal.*, 2017, **49**, 1325–1334.
- 5 E. A. Owen and G. D. Preston, *Proc. Phys. Soc. London*, 1923, **36**, 49–66.
- 6 H. S. Jeon, J. Timosnenko, F. Scholten, I. Sinev, A. Herzog, F. T. Haase and B. R. Cuenya, *J. Am. Chem. Soc.*, 2020, **141**, 19879–19887.
- 7 H. S. Jeon, I. Sinev, F. Scholten, N. J. Divins, I. Zegkinoglou, L. Pielsticker and B. R. Cuenya, *J. Am. Chem. Soc.*, 2018, **140**, 9383–9386.
- 8 N. López and C. Vargas-Fuentes, *Chem. Commun.*, 2012, **48**, 1379–1391.
- 9 B. Hammer and J. K. Nørskov, *Nat. 1995 3766537*, 1995, **376**, 238–240.
- 10 A. Vojvodic, J. K. Nørskov and F. Abild-Pedersen, *Top. Catal. 2013 571*, 2013, **57**, 25–32.
- 11 R. F. W. Bader, *Chem. Rev.*, 2002, **91**, 893–928.
- 12 G. Henkelman, A. Arnaldsson and H. Jónsson, *Comput. Mater. Sci.*, 2006, **36**, 354–360.

